ADVANCED OPTICAL MATERIALS
www.advopticalmat.de

# Metasurface Platform Incorporating Aggregation Induced Emission Based Biosensor for Enhanced Human Serum Albumin Detection

*Qi Hu, Masanobu Iwanaga,* and Youhong Tang**

**Metasurfaces exhibit excellent optical performance to enhance the light–matter interaction of target molecules in biosensing based on its well-optimized nanostructured unit cells. In the meantime, fluorescence (FL) biosensors with aggregation induced emissions (AIE) features also demonstrate outstanding performance in biomarker detection due to their fast response, high selectivity, and low background noise. Nevertheless, extremely low-level analytes are difficult to detect in practical applications since complex urine samples include a number of uncontrolled variables such as impurities, autofluorescence, other urine components, etc. At present, improving optical signal sensitivity of human serum albumin (HSA) detection is always a big challenge to overcome such interference in human urine scenarios. In this work, first an AIE-based FL biosensor TPE-4TA is combined with an all-dielectric metasurface platform to achieve quantitative detection of trace HSA in urine by utilizing biofunctionalization protocols on the silicon (Si) nanostructures. The results indicate significant FL enhancement in the metasurface platform that offers a promising pathway for improving biomarker detection in the future.**

## 1. Introduction

Metasurface is a 2D version of metamaterials that consists of periodic/non-periodic subwavelength metallic/dielectric structures.[1,2] It exhibits the capabilities of concentrating, inhibiting, absorbing, scattering or guiding waves by designing nanoscale cells to achieve dynamic modulation in optics, mechanics, electronics, etc.[3,4] The strong wavefront manipulation is the remarkable characteristic where the unit cells of shape and size, diversified patterns and geometry are tunable and controllable.[5–7] It is precisely based on such characteristics that the attributes of incident light can be customized through light confined mode and localized surface plasmon (LSP) electromagnetic (EM) near-field, thus enhancing light–matter interactions of target molecules.[8,9]

To date, metasurface has been extensively developed in recent decades on the aspects of polarization conversion,[10] wavefront shaping,[11] and controllable radiation.[12] The advancement of metasurface platform has attracted marvelous attention to the applications of biosensing and led to a significant stride toward biomarker detection.[13,14] Oguntoye and his team designed a resonant dielectric photonic Si-nanoantenna metasurface to detect a tuberculosis biomarker CFP-10 peptide and this platform's cost was 87–96% lower than current assays with equivalent sensitivity. The results illustrated that the maximum sensitivity and limit of detection (LOD) were 0.1 μM and 10 pM, respectively.[15] Wang et al. reported an optofluidic silicon-on-insulator (SOI) metasurface that provided multiple nanoscale lateral flow channels to deliver ErbB2 breast cancer biomarkers to the sensor surface. This platform illustrated a resonance mode ≈1550 nm wavelength and LOD for ErbB2 is 0.7 ng $mL^{-1}$.[16] Negm et al. demonstrated a double-resonating metasurface with the characteristic of permittivity asymmetry and geometric asymmetry simultaneously to achieve a thin protein layer sensing. Germanium Antimony Telluride (GST326) ellipse-shaped nanopillars were sensitive to the analyte and showed great robustness of phase transition losses from the amorphous to the crystalline state in the mid-infrared range.[17] In our previous publications, Iwanaga et al. fabricated an effective all-dielectric metasurface fluorescence (FL) biosensor with periodic silicon (Si) nanorods array, which had also successfully detected several biomarkers such as immunoglobulin G (IgG),[18] cancer biomarker (PSA and CEA),[19] cell-free DNA (cfDNA),[20] etc. Specifically, Si or SOI-fabricated metasurfaces possess the

Q. Hu, M. Iwanaga
Research Centre for Electronic and Optical Materials
National Institute for Materials Science (NIMS)
1-1 Namiki, Tsukuba 305-0044, Japan
E-mail: iwanaga.masanobu@nims.go.jp
Q. Hu, Y. Tang
Institute for NanoScale Science and Technology
Medical Device Research Institute
College of Science and Engineering
Flinders University
Bedford Park, South Australia 5042, Australia
E-mail: youhong.tang@flinders.edu.au

The ORCID identification number(s) for the author(s) of this article can be found under https://doi.org/10.1002/adom.202400868



**DOI: 10.1002/adom.202400868**

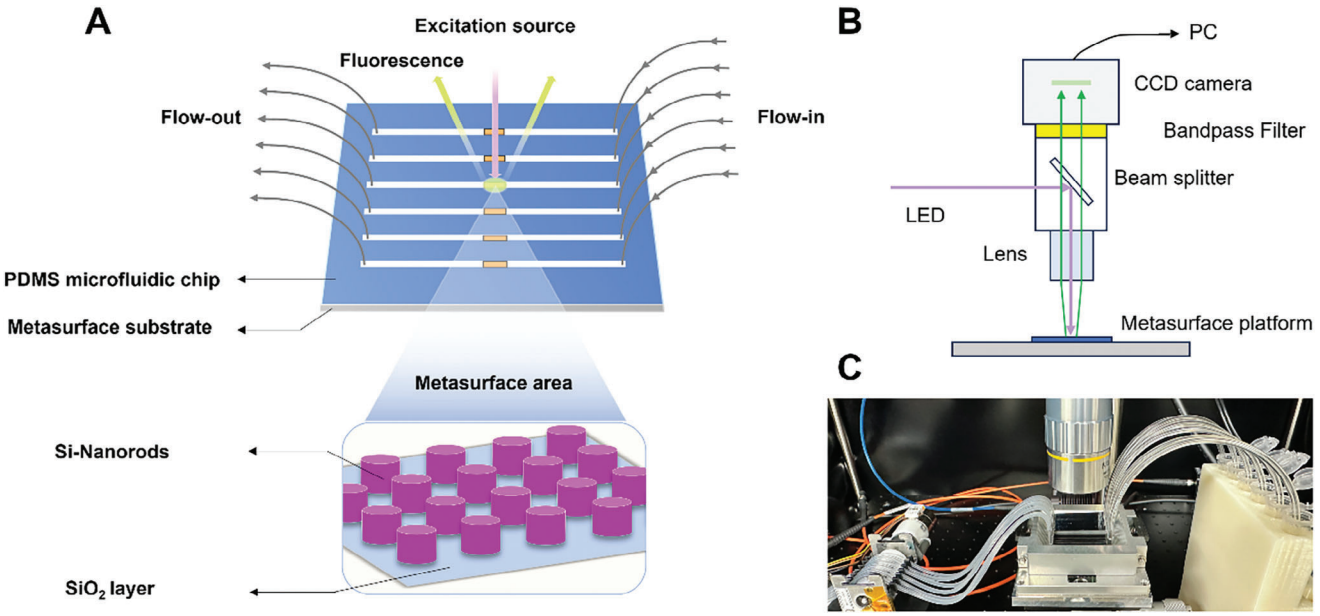


**Figure 1.** A) Schematic diagram of metasurface platform. Inset figure magnifies the nanostructure of metasurface area; B) The schematic diagram of fluorescence (FL) setup for imaging; C) Actual photograph of experimental configuration for human serum albumin (HSA) detection. Sample liquids flow on metasurface platform through inlet (right) and outlet tubes (left) controlled by rotary pump and FL is collected by setup in (B).

tuning adaptability of their optical properties and provide high-quality resonances.[21] When the target analyte enables immobilized or is coated on Si-nanoscale matrices, high refractive index of Si facilitates light modulation,[22,23] resulting in deep light–matter interactions, thereby reflecting on the analyzed peaks. Collectively, these above-mentioned satisfactory results indicate the outstanding capability of metasurface on biomarker nanophotonic detection.

Aggregation-induced emission (AIE) FL biosensors also exhibit excellent detection capabilities in biosensing where the intermolecular interactions restrict the movement of AIE molecules rotors, thus producing an extremely fast and bright FL response through the radiation channel.[24,25] For instance, we have synthesized and reported an AIE-based FL biosensor that achieves the highly efficient detection of human serum albumin (HSA) with a wide linear dynamic range 0–1000 mg $L^{-1}$ and LOD 0.253 mg $L^{-1}$.[26] However, HSA measurement using AIE FL biosensors has always faced considerable challenges in human urine scenarios owing to unpredictable reasons regarding the complexity of urinary excrement. For starters, it has been discovered that albumin excretion varies greatly across individuals, with a typical within-person coefficient of variation (CV) of 40–60%,[27] which leads to a broad concentration extension of urinary HSA from extremely low to high depending on individual differences. In addition, the urine matrix is made up of a variety of organic and inorganic compounds, ranging from low-molar mass molecules to polymers.[28] It could also contain cells and bacteria that have the ability to rapidly change the composition of urine.[28] On the basis of this background, undesirable FL enhancement or quenching will be further triggered because of the interference of numerous impurities,[29] autofluorescence,[30] other urine components,[28,31] etc. Consequently, it is inevitable to overestimate or underestimate HSA content, leading to inaccurate readings, especially at an extremely low-level.[32] Not only that, but the optical signal is also hardly detectable due to small amplitude of light absorption when HSA concentration is low, which requires high detection accuracy by boosting sensitivity or reducing background noise. To address these issues with complex bio-samples in practical applications and evaluate the biomarker detection performance of metasurface in biosensing, herein, we first report nanophotonic all-dielectric metasurface platforms coupled with AIE featured FL biosensors for achieving the enhanced detection of HSA. This platform integrates a microfluidic system and a metasurface substrate to enable analyte delivery and the monitoring/detection of FL enhancement in real-time with the outstanding characteristics of high throughput, good reusability and low reagent consumption, as shown in **Figure** 1A. Under the FL setup (Figure 1B,C), the results from human urine samples show that our proposed metasurface has significant potential as a biomedical chip-based platform for providing a promising pathway of enhancing sensing and biomarker detection quantitatively.

## 2. Results and Discussion

### 2.1. Optical Properties of Metasurface Platform

The optical optimization of the metasurface has a history, which was reported in previous publications.[1–3,33–35] In principle, FL-intensity enhancement is a consequence of multiple control of photoexcited states;[33–35] that is, FL enhancement factor is equal to the product of excitation efficiency, inner quantum yield, and FL-emission efficiency (namely, Purcell factor). One of the keys is to the FL-emission efficiency, which was optimized by adjusting a particular resonant mode of the metasurface (i.e., a reflectance peak in **Figure** 2B) to the wavelength of FL. This was conducted

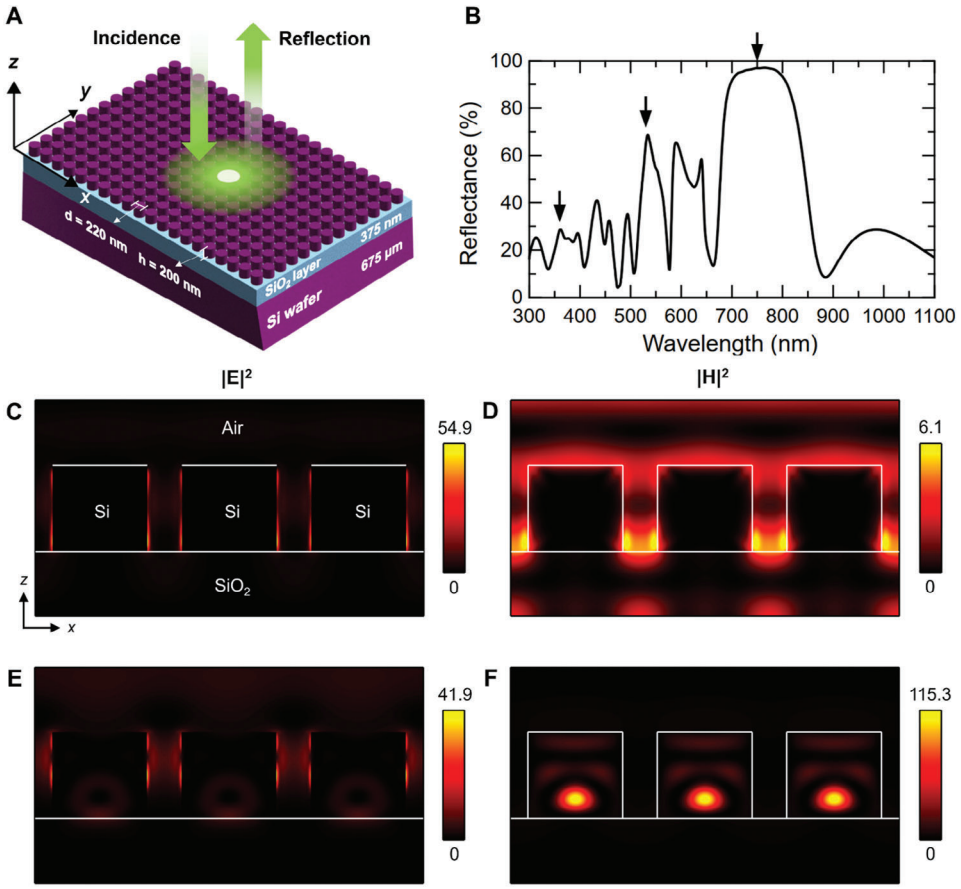


**Figure 2.** A) 3D illustration of metasurface of Si nanocolumn (diameter d = 220 nm, height h = 200 nm) array forming a square lattice of periodicity 300 nm. B) Simulated reflectance spectrum at the normal incidence in a wide wavelength range from the UV to the near infrared. C,D) Electric and magnetic field intensities ($|E|^2$ and $|H|^2$), respectively, excited at 360 nm, which is indicated by an arrow in Figure 2B. This xz-section was set to cut through the center of the Si nanocolumns. E,F) Electric and magnetic field intensities, respectively, shown in the xz-section view similar to (C,D) and excited at 530 nm, indicated by an arrow in Figure 2B. Incident field was set to be unity, that is, $|E_{in}|^2 = 1$ and $|H_{in}|^2 = 1$. Color bars indicate the field intensities. White lines show the interfaces of the Si nanocolumns with air and the underlying $SiO_2$ layer.

by tuning the diameter and height of the Si nanocolumns.[35] Besides, the periodicity of the metasurface was set to a reasonable value, in accordance with the diameter of the Si nanocolumns. Thus, the present metasurface has a set of optimized structural parameters, based on the previous studies.[18,35] In this case, the optical structural design of metasurface is suitable for AIE FL biosensor TPE-4TA to achieve FL signal enhancement at green wavelengths ≈530 nm. Figure 2A shows the dimension parameters of SOI-nanorod metasurface with the thickness of a base Si wafer 675 μm and $SiO_2$ layer 375 nm, respectively. Si nanocolumns consisting of diameter of 220 nm and height of 200 nm forms a square lattice of 300 nm periodicity. Normal incident light propagates from the air to the metasurface, ensuring that the vector of the electric field is perpendicular to the incidence plane. Furthermore, the reflectance spectrum, as shown in Figure 2B, was numerically computed in the configuration of Figure 2A, exhibiting reflection peaks or dips according to the resonances of metasurface. A reflectance band of 30% is generated at 360 nm which is the excitation wavelength for TPE-4TA, whereas the reflection response at 530 nm reaches up to 70% with a single sharp peak significantly. A high reflectance exceeding 90% also observed between 700–800 nm, which originates from the magnetic dipole resonance (Figure S1, Supporting Information). Figure S2 (Supporting Information) shows simulated and measured reflectance spectra, respectively. Overall, the two spectra agree with each other in the spectral shapes. Since the spectrometer allowed us to measure reflectance at 5 degrees and more, we set the incident angle to be 5°, which is close to the normal incidence, and, indeed, verified that the simulated spectrum in (A) is approximately the same as the spectrum in Figure 2B. Importantly, the main feature regarding reflectance peaks at 360 and 530 nm, which was related to the FL enhancing effect in this study, was reproduced in the measured reflectance spectrum (B). The incident polarization was set to s polarization, which means that, when plane of incidence is the *xz* plane, the incident electric-field vector is parallel to the *y*-axis. Besides, we mention that some interference signatures at 840–1050 nm came not from the metasurface itself but from the optical configuration in the spectrometer. Afterward, to visualize the underlying mechanism of the FL enhancement induced by the Si nanocolumns, resonant EM field distributions are investigated in Figure 2C–F. The intensities of electric fields ($|\mathbf{E}|^2$, Figure 2C)

and magnetic fields ($|\mathbf{H}|^2$, Figure 2D) excited at 360 nm are reinforced to 54.9 and 6.1, respectively, in comparison with the incident field intensity of 1.0. These EM-field distributions are dark inside the Si nanocolumns and indicate that the incident light was absorbed in the Si nanocolumns. However, the electric field at the outermost surface is highly enhanced at the sidewall of the Si nanocolumns and is not significantly reduced at the top of the Si nanocolumns. At the wavelength of 530 nm, the electric field intensity decreases at 41.9 slightly but this strong electric field distributions shift toward the upper part of the Si nanocolumns on which the majority of FL-labeled HSA analytes tend to be immobilized (Figure 2E). Notably, the magnetic fields are significantly enhanced up to 115.3 inside Si nanocolumns as Figure 2F shows, which indicates that this resonance is a magnetic mode (specifically, a higher magnetic mode than magnetic dipole mode), corresponding to the high-reflectance resonance at 530 nm in Figure 2B. The reinforced resonant EM fields are advantageous to transit electric dipole in FL molecules,[35] thus contributing to enhanced FL emission at the outermost surface of the Si nanocolumns. The numerical calculation was based on rigorous coupled-wave analysis and scattering matrix algorithm.[36]

### 2.2. Detection Strategy and Binding Affinities on Metasurface Platform

The detection strategy is to utilize biofunctionalization protocols of binding molecules, labeled antibody (Ab), and target analyte for achieving multi-level immobilizations on metasurface (**Figure 3A**). After initial phosphate-buffered saline (PBS) flow, the binding molecules of Cys-streptavidin (Cys-SA) flow through the microfluidic paths onto the metasurface regions where a uniform and stable physiosorbed layer is formed directly by the interaction between streptavidin and the silica shell of nanocolumns.[37] Next, HSA antibodies labeled with biotin (Biotin-HSA Ab) are bound to the Cys-SA through the fast and strong non-covalent protein-ligand interactions, and this formed complex biolayer provides a good high-density binding platform for HSA. Furthermore, when tetrazolate nitrogens from FL biosensors TPE-4TA bind with polar dominant-contacting lysine residues (Lys) in HSA binding conformation through hydrogen bonding and electrostatic interactions, triggered restriction of intramolecular movement effect lights up HSA.[38] Afterward, pre-bound products of HSA and TPE-4TA can be captured persistently through antibody-antigen reaction. Notably, PBS rinsing is compulsory to remove unbound parts after immobilization at each level. Besides, the results in Figure S3 (Supporting Information) demonstrate that the binding sequence of TPE-4TA affects the final FL response. Two pre-bound products ([HSA+TPE-4TA] and [HSA Ab+HSA+TPE-4TA]) possess the strongest FL intensities in this protocol compared to the case where TPE-4TA is individually immobilized on HSA in the last step. The potential reason for the FL-intensity differences is the inward orientation of HSA as big biological molecules when immobilized. The binding sites of endogenous and exogenous substances are mainly located in subdomain IIA and IIIA on HSA tertiary structure[39–41] where IgG binding positions of ligands on HSA are localized precisely in Domain III.[42,43] Nevertheless, the favorable binding positions of ligands between HSA and TPE-4TA are found in the intersection of Domain I and Domain III.[38] Once HSA immobilizes onto its Ab successfully, Domain I and III of HSA mainly face the surface of Si nanocolumns. The presence of steric hindrance may limit TPE-4TA movement by crossing directly into the interface of Domain I and III, thereby the binding opportunities between HSA and TPE-4TA will be further reduced due to immobility of adaptive spatial conformation of HSA-HSA Ab (Figure S4, Supporting Information). However, the prepared mixing solution of HSA and TPE-4TA beforehand can be fully reacted to completely avoid this binding loss. In short, the whole designed biofunctionalization protocol indicates that the detection strategy is feasible and optimal for binding identification, stability, and intensity, which has been validated from subsequent experimental results.

In order to ensure that the preset immobilizations can proceed as the desired protocols, the surface plasmon resonance (SPR) measurement was conducted to evaluate the effectiveness of immobilization quantitatively as shown in Figure 3B. The measurement was conducted on a flat gold surface where SPR is induced. The initial flow of PBS at 10 μL $min^{-1}$ for 10 min is the highest priority step to clean the gold film surface and maintain unobstructed microfluidic paths. Next, Cys-SA, Biotin-HSA Ab, and the mixing solutions of HSA and TPE-4TA are flowed at 10 μL $min^{-1}$ for 10 min, respectively. Furthermore, each binding stage contains a standard rinse with PBS for 10 min to remove residual reagents from the previous step. The results at the steady state indicate that binding affinity reflects on a quantity, ΔRU, defined as absorbent mass per unit area in the scale of pg $mm^{-2}$. As the sequential immobilizations accomplish, ΔRU continues to increase with three binding stages, which are 1303.8 of Cys-SA immobilization (Molecular weight, $M_{Cys\text{-}SA}$ = 17.9 kDa), 1694.2 of Biotin-HSA Ab immobilization ($M_{Biotin\text{-}HSA\ Ab}$ = 69 kDa) and 281.5 conjugates of HSA and TPE-4TA ($M_{HSA+TPE\text{-}4TA}$ = 67 kDa), respectively. The inset figure in Figure 3B represents the difference of HSA with/without TPE-4TA in binding response. Compared with HSA solution only, the binding ratio of HSA+TPE-4TA increases by 34%, which is attributed to the ligands binding of TPE-4TA through hydrogen bonding and electrostatic interactions. Based on the analysis of BIACORE, the theoretical binding capacity of TPE-4TA as small molecules on gold surface can be calculated using the following Equation 1:

$$R_{TPE-4TA} = \frac{M_{TPE-4TA} \times R_{HSA} \times S_r}{M_{HSA}}\ (\mathrm{RU}) \tag{1}$$

where $M_{TPE-4TA}$ and $M_{HSA}$ represent the molecular weight of TPE-4TA and HSA, respectively; $R_{HSA}$ represents the binding capacity of immobilized HSA and $S_r$ refers to the stoichiometric ratio between TPE-4TA and HSA.

The result indicates that 95.7 of the measured binding response of TPE-4TA are 24 times more than the theoretical estimate. This increase could be explained by the AIE phenomenon since numerous FL molecules of TPE-4TA aggregate into the structural cavity of HSA.

Moreover, the immobilized molecular density is evaluated by the Equation 2:

$$D_A = \frac{M_A}{R_A \times N_A}\ \left(1\ \text{molecule for nm}^2\right) \tag{2}$$

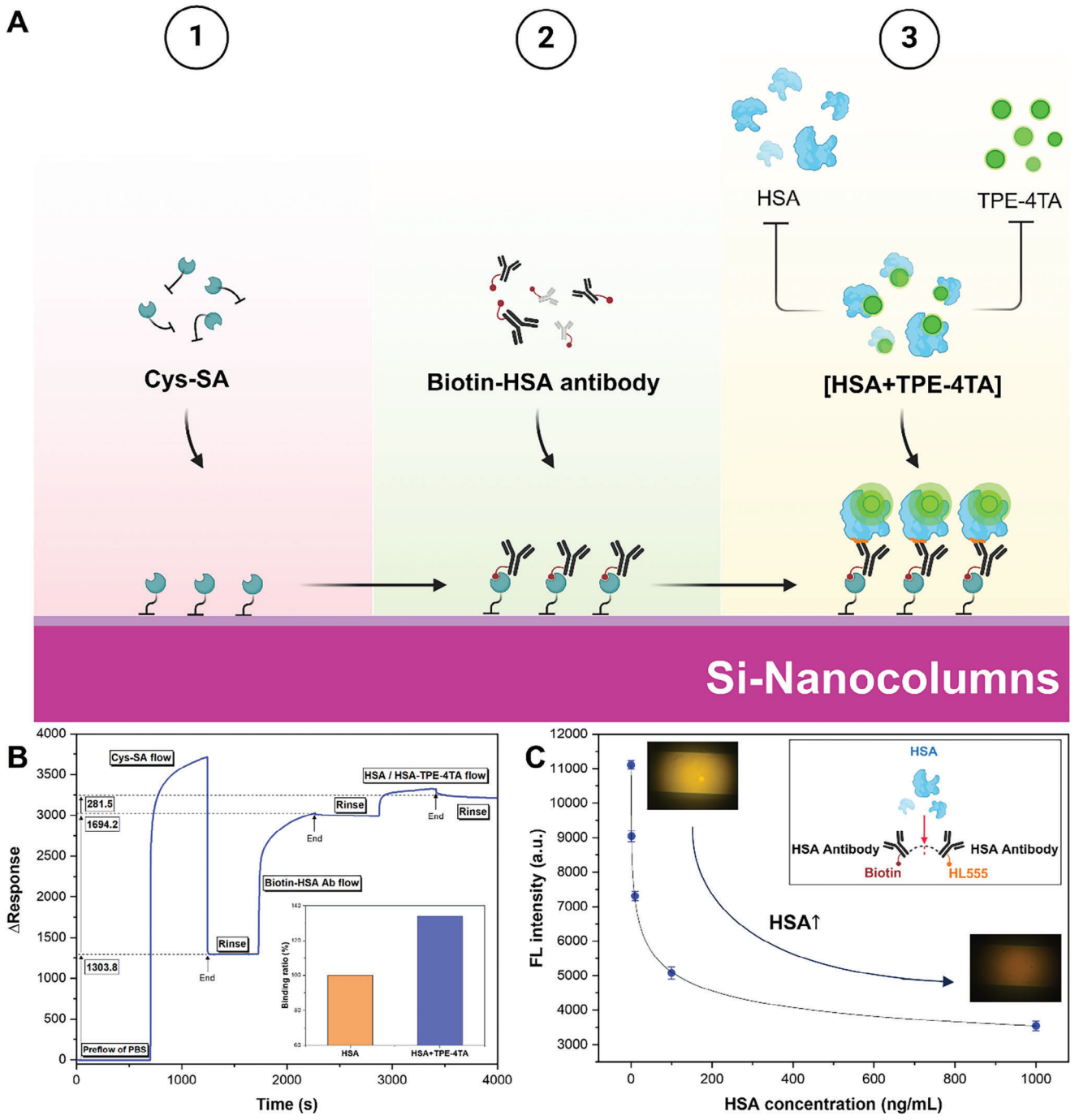


**Figure 3.** A) Schematic diagram of multiple immobilizations on Si nanocolumns; B) Binding response of immobilizations on an Au-film sensor chip using surface-plasmon-resonance instrument. Inset: the difference of binding ratio between HSA and the mixture of HSA + TPE-4TA in the final immobilization step; C) Non-specific absorption between 2 μg $mL^{-1}$ Biotin-HSA Ab and 5 μg $mL^{-1}$ HL555-HSA Ab with HSA concentration varying. Inset: the change of FL efficiency with different concentrations of HL555-HSA Ab.

where $D_A$ represents the immobilized molecular density of the analyte; $M_A$ represents the molecular weight of the analyte; $R_A$ represents the binding capacity of the analyte and $N_A$ is the constant of Avogadro.

The result shows that one molecule of Cys-SA, Biotin-HSA Ab and conjugates of HSA and TPE-4TA are situated on an average square surface area of 4.61 × 4.61, 8.20 × 8.20, and 19.9 × 19.9 $nm^2$, respectively, indicating this multi-level immobilization strategy is feasible and can be also applied in our platform effectively.

The indirect verification of immobilization is also carried out through non-specific Ab-Ab absorption as shown in Figure 3C.

In this case, the same species of HSA Abs have been labeled individually with two different moieties: biotin and FL-label HyLite Flour 555 (HL555). The flowing order of samples is as follows: Cys-SA, Biotin-HSA Ab, HSA, and HL555-HSA Ab then rinse is performed after each sample flow. Concretely, HL555 labeled HSA Abs emit FL at the peak of 570 nm and they will be absorbed onto Biotin-HSA Abs in metasurface area that has not reacted with HSA yet, hence being forced to dock on the metasurface likewise. When different concentrations of HSA are already fixed on 2 μg $mL^{-1}$ Biotin-HSA Abs, FL quenching effect occurs as HSA concentration increases upon extra introduction of 5 μg $mL^{-1}$ HL555 labeled HSA Ab into the microfluidic paths, which proves that antibody-antigen reactions with higher priority interrupt Ab–Ab nonspecific absorption (Inset graph of Figure 3C). The results illustrate that FL intensities reach the strongest value in the absence of HSA meanwhile it descends by 68.1% when HSA concentration reaches 1000 ng $mL^{-1}$. Figure S5 (Supporting Information) reveals that the concentration of HL555-labeled HSA Ab is positively correlated with its FL efficiency under this nonspecific absorption. The inset figure in Figure S5 (Supporting Information) indicates that the introduction of HSA is the primary factor for this FL quenching effect. Consequently, multi-level immobilization can also be confirmed indirectly.

### 2.3. FL Kinetics on Metasurface Platform

The FL kinetics behavior of AIEgen TPE-4TA in HSA detection under the modulation of metasurface platform is evaluated in this section. TPE-4TA has excellent FL response toward HSA and its concentration effect has been optimized (Figures S6 and S7, Supporting Information). Its good selectivity toward HSA excludes potential interference from biomolecules over various proteins with isoelectric points ranging 1–10 in buffer solution.[38] **Figure** 4A shows an excellent photostability of HSA+TPE-4TA conjugate within 2 h, which allows multi-level immobilizers to generate FL persistently on the metasurface. Moreover, FL intensity is positively related to HSA concentration as displayed in Figure 4B. FL enhancement in the microalbumin range is divided into two phases: a sharp phase (0–20 μg $mL^{-1}$) and a slow phase (20–160 μg $mL^{-1}$). The slowing trend indicates binding capabilities of Biotin-HSA Ab are approaching their maximum limitation. The steady FL intensities near 160 μg $mL^{-1}$ describe that the fixed amount of HSA and TPE-4TA conjugates has been regionally saturated on metasurface. Significantly, the metasurface platform remains ultra-sensitive toward the trace of HSA (< 20 μg $mL^{-1}$) where FL signal climbs rapidly at 82% of maximum response when HSA content jumps toward 20 μg $mL^{-1}$. To further explore the extent to which the metasurface platform contributes to FL amplification, two other platforms (i.e., microplate platform and microfluidic platform) are also established for horizontal comparison and the corresponding linear fittings of three platforms are plotted in Figure 4C and Figures S8 and S9 (Supporting Information). The microplate platform is composed of the conventional transparent polystyrene materials and microfluidic platform possesses the same construction as metasurface platform without Si-nanocolumns. In Figure 4D, 39% and 136% FL enhancement of HSA detection are observed in microplate platform and microfluidic platform respectively, however, emitted FL boosts up to 1001% under the light-confined mode in the metasurface platform. Through comparison of three platforms (Figure 4E), FL signal of the metasurface platform and the microfluidic platform are 7.93-fold and 1.70-fold stronger than that of the microplate platform respectively. Obviously, FL regulation of metasurface is superior to the other two platforms. We also note that the numbers of the FL molecules involved in these measurements are the least in the metasurface platform because the PBS rinse removed the unbounded FL molecules. Thus, net FL-detection efficiency is far superior in the metasurface platform to the other microplate and microfluidic platforms.

On top of that, the practical evaluation in the application of human urine is investigated among three platforms to verify feasibility of sensing augmentation. In urinary FL analysis, autofluorescence is induced inevitably under UV light and leads to FL overlap within the detection scope of 529–571 nm (Figure S10, Supporting Information). Hence, treated urine samples diluted 80 times with PBS buffer are employed as the standard to eliminate the impact of auto-FL as efficiently as possible (Figure S11, Supporting Information). PBS buffer also maintains diluted urine samples into a neutral environment avoiding the potential impact of changes in urinary pH on FL measurements. Additionally, the robustness of TPE-4TA has already been proved in slightly acidic environment, and main urinary components, such as urea, uric acid, creatinine, etc., do not interfere assay sensitivity of HSA.[38] Validation from the commercial kit shows HSA level of 45.8 μg $mL^{-1}$ in the urine samples and this concentration can be calculated independently by referring to the standard curves established in three platforms to obtain 40.7, 41.9, and 43.8 μg $mL^{-1}$ with recovery rates of 88.9%, 91.5%, and 95.6% respectively (Table S1, Supporting Information). Through systematic measurements presented in Figure 4F, the FL retention rate refers to the percentage variations in detectable FL signals from intense to dimmed at extremely low HSA concentrations as the dilution ratio increases. First, the FL retention rates of three platforms are 100% in the initial phase (80x diluted urine samples) and drop toward 80% with doubling of the dilution ratio (160x). When the dilution ratio is adjusted to 320x, the microfluidic and metasurface platforms retain their 70%, while the microplate platform experiences a dramatic decline to 29%. At this time, the FL retention rate of the microplate is less than half of that of the other two platforms. Next, 7%, 18% and 38% FL retention rates are recorded under the dilution ratio of 640x where metasurface platform is 2.1 folds and 5.4 folds more intense than the microfluidic and microplate, respectively. After that, the metasurface maintains 27% of FL signal with further dilution (1280x) whereas the microplates and microfluidics almost lose it completely (2%). Similar circumstances still persist until the final phase of 2560x with near 10% retention rate in metasurface. Moreover, microplate, microfluidic and metasurface platforms have 300 ng $mL^{-1}$ (LOD1), 150 ng $mL^{-1}$ (LOD2), and 18.75 ng $mL^{-1}$ (LOD3) as their respective detection limits, corresponding to the FL retention rate of 80%, 70% and 9% respectively. The above results of FL retention rate change are consistent with the performance of LODs in three platforms. Finally, the sensitivity level is expressed as: metasurface > microfluidic > microplate. The metasurface platform can effectively amplify the FL signal at extremely low concentrations of HSA in human urine environment. FL retention rate is still detectable even if

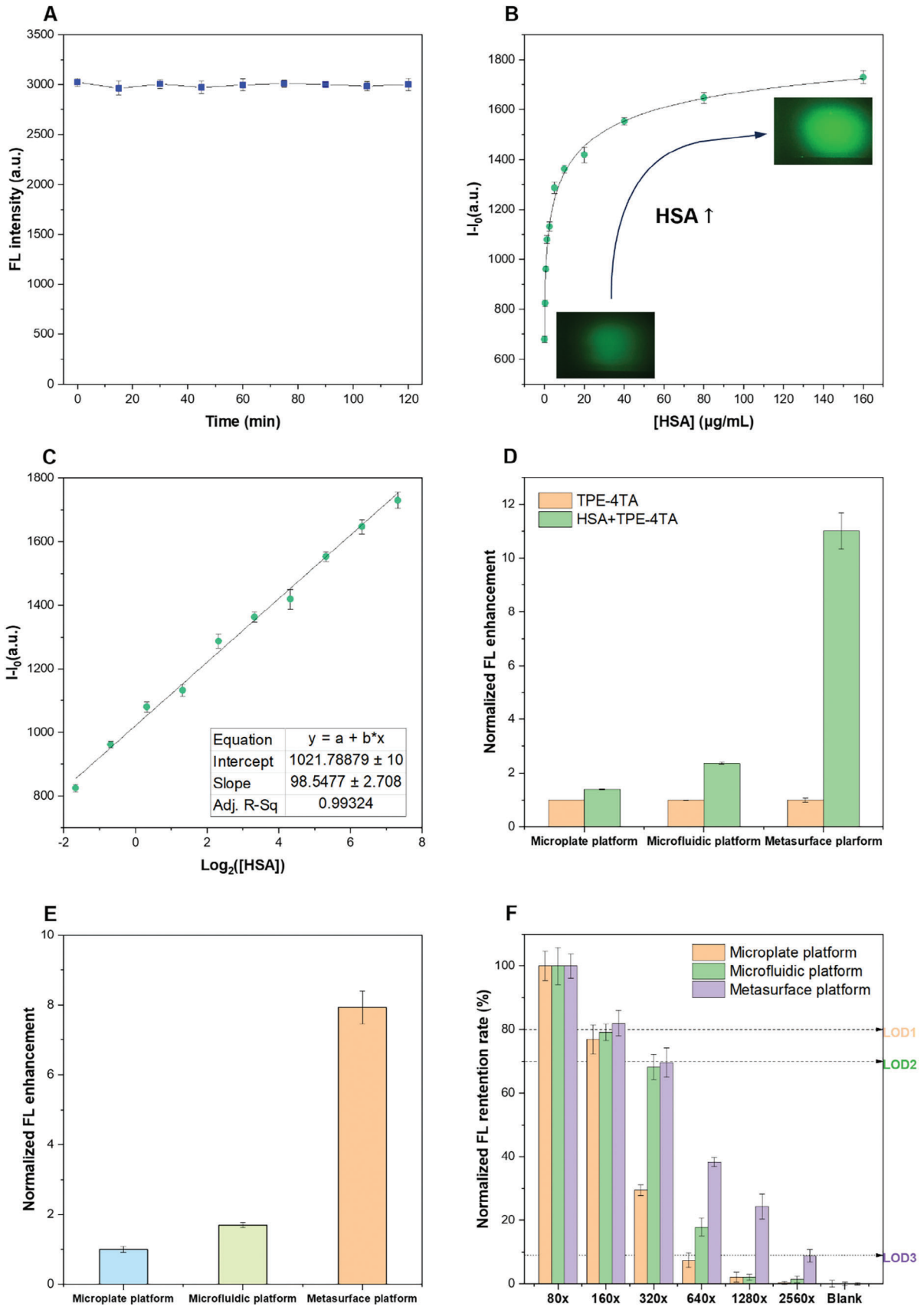

urine specimens are diluted by 2560 times, which fully illustrates that Si-nanocolumn matrices which enable HSA to immobilize are the primary reason for producing FL enhancement.

### 2.4. Underlying Mechanisms on Metasurface Platform

After understanding the optical properties, binding affinities, and FL kinetics of metasurface platform throughout the dynamic sensing process, the potential mechanism can be explained in **Figure 5** displayed with the comparison of three models. Initially, large-scale wells located on microplate platforms enable numerous conjugates of HSA and TPE-4TA to freely move in multi-dimensional directions. Uniformly dispersed FL molecules are hardly restrained in camera zone, resulting in the limited FL signal in large liquid dimensions. Remarkably, microfluidic and metasurface platforms further compress the scope of FL activities along the height direction, thus enabling us to acquire the focused FL images, which aligns with the results presented in Figure 4E. More significantly, the Si nanocolumns allow FL molecules to be stacked in a non-uniform manner within an extremely small area and a local enrichment state occurs, thus enhancing FL output. Particularly, the reinforced effect of resonant EM fields further amplifies FL emission of HSA+TPE-4TA from the outermost surface of Si nanocolumns through multi-level immobilizations. Moreover, the results from FL kinetics (Figure 4B) reveal that FL enhancement is subject to the total fixed number of conjugates of HSA and TPE-4TA in metasurface area. FL molecules immobilization reaches its saturation when the concentration of HSA is excessive (>160 μg $mL^{-1}$). The amplifying effect can only occur on the bound sections and does not cause promotion with HSA concentration continuing to increase any longer. Conversely, the microalbumin or trace range does not have the saturation effect, which is the reason why the metasurface is more significant for it.

### 2.5. Future Prospects on Metasurface Platform

This research offers a feasible strategy to achieve enhanced HSA detection using AIE FL biosensor incorporating with metasurface platform. Through the reinforced resonant EM fields of Si nanocolumns, optical signal sensitivity of analytes can be amplified, which is particularly significant in the presence of many interferences in the urine scenarios. Improved LOD meets the higher standard requirements of HSA detection at a low level. Besides that, the removal of HSA from human urine for enhancing sample loading capabilities in analytical methods becomes a promising pathway to identify low-abundant proteins and improve their detection sensitivity. To be more specific, urine contains thousands of different types of proteins, while HSA is one of the main proteins as the high-abundant proteins. At present, more than 3400 individual proteins have been found in urine that could become potential biomarkers for different diseases and the majority of them belong to low-abundant proteins.[44,45] The masking effect of HSA poses an impeding factor in urine for discovery/screening of less-abundant proteins. Si nanocolumns enable to deplete existing HSA content efficiently to act as the function of filtration. The superior optical properties provided by the metasurface platform are apparently beneficial for monitoring downstream process analysis of HSA removal.

Our metasurface platform also provides a universal microfluidic design to be biofunctionalized for targeted biomarker detection via the combination of standard streptavidin-biotin model, immunobinding and FL labeling, which is fully capable of applying to other biomarkers. First, the array of Si-nanocolumns constructed on SOI substrate has a larger surface area on which biomolecules are allowed to immobilize. Second, this platform can achieve high reflectance in visible wavelength range to be compatible with optical properties of target objects by turning radius and periodicity. Third, FL molecules specific to target biomarkers are selected carefully to ensure that steady output of optical signal will be turned on only after multi-level immobilization is completed successfully. More significantly, the running cost can be reduced dramatically because our metasurface substrates are reusable by washing.

All-dielectric metasurface platform has been illustrated on biomarker detection in biosensing with extraordinary optical characteristics that may lead to better sensitivity, higher throughput, and more significant specificity for extremely low-level analytes in the future. The performance of several instances of all-dielectric metasurface platforms based on microfluidic FL sensing is summarized in this section as shown in **Table 1**. As metasurface platform becomes better explored, it will have a potential promotion on biomarker detection in the medical diagnosis criterion to be a higher standard.

## 3. Conclusion

This designed all-dielectric metasurface platform shows a resonance of 70% reflection response at 530 nm and can enhance FL emission at the outmost surface of Si nanostructures owing to the significant amplification of its resonant EM field. Subsequently, the multi-level immobilization as a detection strategy successfully implements strong high-density bindings of FL molecules on metasurface area. FL kinetics results prove its good photostability and a good dynamic range of 0–160 μg $mL^{-1}$ especially ultrasensitive to the trace HSA. In the comparison of three platforms, metasurface platform is superior to microplate and microfluidic platforms, which exhibits 1001% FL enhancement, and its FL

**Figure 4.** A) Stability of FL in HSA detection within 2 h using the metasurface platform; B) The correlation of HSA and TPE-4TA from 0 to 160 μg $mL^{-1}$ using the metasurface platform. Inset graphs are change in FL images at 0 and 160 μg $mL^{-1}$; C) The corresponding standard curve of TPE-4TA for HSA detection in the range of 0–160 μg $mL^{-1}$ using the metasurface platform based on (B); D) The difference of FL response with/without HSA in each of platform; E) The comparison of FL enhancement among the microplate platform, the microfluidic platform and the metasurface platform; F) FL retention rate between three platforms in urine scenarios with different dilution ratios where dilution ratios refer to total volume/treated urine volume with PBS buffer as diluent. Three broken horizontal lines represent corresponding LODs in different platforms (LOD1: the microplate platform (orange), LOD2: the microfluidic platform (green), LOD3: the metasurface platform (purple)).

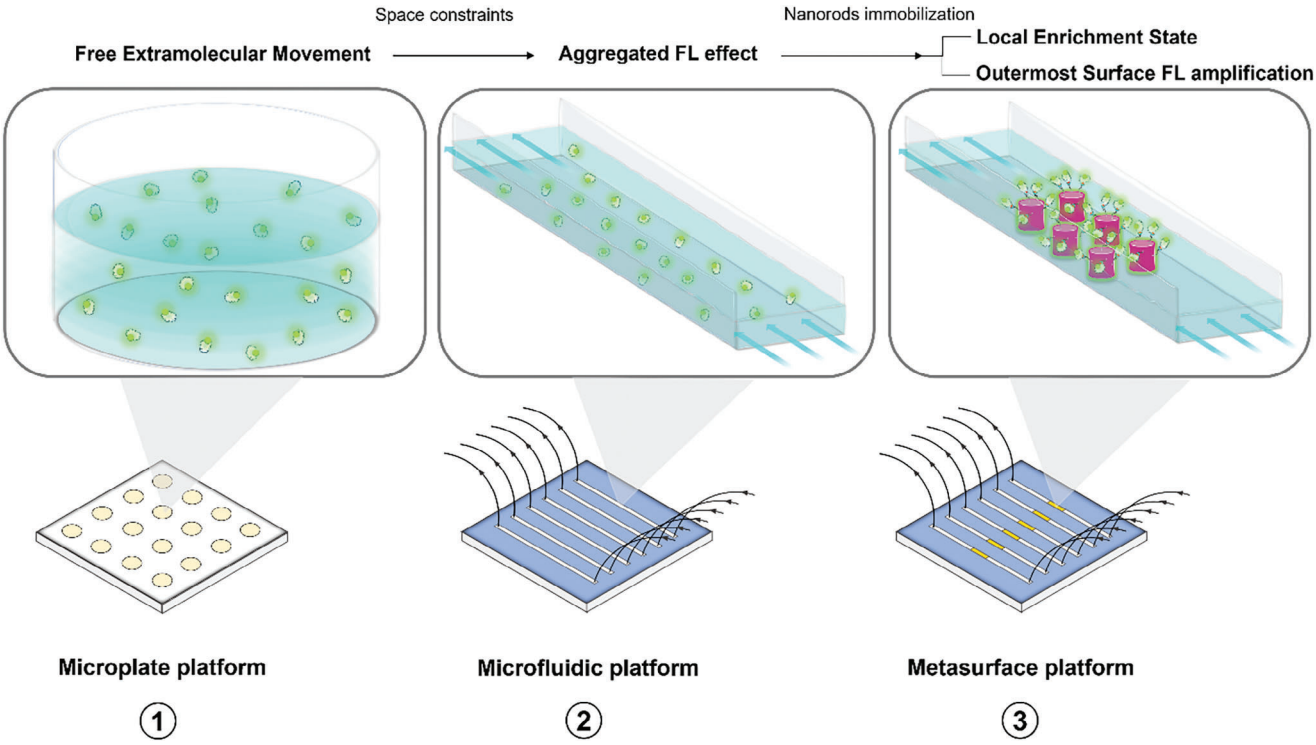


**Figure 5.** Potential mechanism of the metasurface platform compared to the microplate and microfluidic platforms under their nanostructures.

signal is 7.93-fold and 4.69-fold stronger than the others. Furthermore, the results in urine testing demonstrate the highest recovery rate (96%), the lowest LOD (18.75 ng mL$^{-1}$) and the biggest FL retention rate (9%) in urine up to 2560 times diluted among three platforms. The underlying mechanism concludes that a local enrichment state on the metasurface area and space constraints from microfluidic paths are the main reasons for enhancing FL emission. In summary, the AIE-based FL biosensor incorporating a metasurface platform can effectively achieve FL enhancement in HSA detection. The combination of AIE fluorogens and metasurface platform opens up a new route for biosensing in real scenarios.

## 4. Experimental Section

*Materials and Instruments*: The FL biosensor TPE-4TA had been synthesized according to previous publications.[38] Human serum albumin (HSA) was purchased from Sigma–Aldrich (A1653-500MG, Germany). Biotin labeled HSA antibody (Biotin-HSA Ab) was purchased from Abcam (ab27632, purified, UK). Cys-streptavidin (Cys-SA) was purchased from Click Biosystems (PRO1005, Richardson, USA). Raw human urine samples were purchased from LEE BioSolutions (991-03-S, USA). Phosphate-buffered saline (PBS) and PBS-Tween 20 (PBS-T) were purchased from Fujifilm Wako Pure Chemical, Japan (164-25511 and 163–24361, respectively). Nanosep Centrifugal devices were purchased from Pall Life Sciences (OD300C34, USA). HiLyte Fluor 555 (HL555) Labeling Kit was purchased from Dojindo Molecular Technologies (LK14, Japan) and the

**Table 1.** Summary of FL detection of biomarkers on the metasurface platform. AF555 denotes Alexa Flour 555, HL555 HyLite Flour 555, and HEX a FL probe on DNA.

| No. | FL component | Biomarker | Performance | | Refs. |
|---|---|---|---|---|---|
| | | | Dynamic range | LOD | |
| 1 | TPE-4TA | HSA | 0–160 μg mL$^{-1}$ | 18.75 ng mL$^{-1}$ | This work |
| 2 | AF555 | IgG | 5–2000 pg mL$^{-1}$ | 5 pg mL$^{-1}$ | [18] |
| 3 | HL555 | PSA and CEA | 0.16–1000 ng mL$^{-1}$; 0.002–25 ng mL$^{-1}$ | 1 ng mL$^{-1}$; 0.002 ng mL$^{-1}$ | [19] |
| 4 | HL555 | COVID-19 glycoprotein peptide and corresponding Ab | 0.16–100 ng mL$^{-1}$; 6.25–100 ng mL$^{-1}$ | 0.64 pg mL$^{-1}$; 1.56 ng mL$^{-1}$ | [46] |
| 5 | HEX | cfDNA | 0–2 fM | 0.488 aM | [20] |
| 6 | HEX | SARS-CoV2 | 5–4000 aM | 5.86 aM | [47] |

labeling operation was done according to standard protocols. Human Albumin SimpleStep ELISA Kit was purchased from Abcam (ab227933, UK) and the operation procedure followed the standard instructions in the manual.

An all-dielectric metasurface manufacturing procedure was carried out through the use of electron-beam lithography and dry etching on SOI wafers according to our previous publication.[18,48] The six metasurface regions in this investigation were distributed in the middle of each substrate with the dimension of 45 × 45 $mm^2$, corresponding to six microfluidic flow in-out channels, as seen in Figure 1A. Notably, the metasurface substrates could be reused after being washed with a complex acid solution ($H_2SO_4 + H_2O_2$).

The FL setup is illustrated in Figure 1B. The Light-emitting device was acquired from Thorlabs (M365FP1, USA). 10× objective lens was acquired from Mitsutoyo (M Plan Apo, Japan). 16-bit FL images were recorded by an uncooled CCD camera (Infinity-3S, Teledyne-Lumenera, Canada). FL spectra were measured by Spectrofluorometer (FP-8500, Jasco International, Japan). The binding affinity was obtained from the surface plasmon resonance instrument (SPR, BIACORE-X100, General Electric Healthcare, USA).

*Preparation of Samples*: AIE FL biosensor TPE-4TA solution (1000 μg $mL^{-1}$) as the stocking solution was dissolved in PBS buffer and stored at 4 °C in the dark environment. Stocking solution would be diluted freshly with PBS buffer to 20 μg $mL^{-1}$ in every experiment unless otherwise noted. The freshly made HSA solution was formulated to 1000 μg $mL^{-1}$ in PBS buffer and diluted to the required concentration of 0–1000 μg $mL^{-1}$ with a specific concentration gradient. 200 μg $mL^{-1}$ of Cys-SA stocking solution and 1 mg $mL^{-1}$ of Biotin-HSA Ab were diluted to 20 and 5 μg $mL^{-1}$ with PBS buffer for daily use, respectively. PBS-T buffer was diluted with PBS buffer (pH 7.4) three times for rinsing use. Mixing solutions of HSA and TPE-4TA were incubated for 10 min before use.

In the Results Section 2.2, in order to ensure that all components were fixed tightly on the gold thin film, Cys-SA, Biotin-HSA Ab, HSA, and TPE-4TA were all formulated to relatively high working concentration of 20 μg $mL^{-1}$ during the experiments of binding response. For non-specific absorption, HL555- HSA antibodies were set to 0–5 μg $mL^{-1}$ in Figure 2C.

In human urine testing, raw urine samples (991-03-S, Lot. 18-06-615, Lee Biosolutions, MO, USA) would be thawed from −20 °C to room temperature. Afterward, centrifugal filters with 300K Omega film were used to centrifuge for 10 min with the rotation speed of 120 × 100 g and this operation must be repeated three times for each experiment until a sufficient amount of treated urine was collected for further use. Finally, the treated urine could be prepared into different urine samples through specific dilution factors with PBS. The mixing solutions of urine samples and TPE-4TA were incubated for 10 min before measurement.

*Preparation of Metasurface Platform*: The metasurface platform was a dynamic measurement that composed of a self-absorbed pair of a metasurface substrate and a polydimethylsiloxane (PDMS) microfluidic chip (thickness = 2 mm) that had six flow-in and flow-out independent microfluidic channels. These microfluidic paths (height = 30 μm) were connected with tubes and the flowing speed could be controlled by a rotary pump (RP-6R01S-5A-DC3V, Takasago Fluidic Systems, Japan). In the meanwhile, this metasurface substrate was a three-layer planar structure (from top to bottom) consisting of the Si-nanocolumns array (with a diameter of 220 nm, a height of 200 nm, and a period of 300 nm), a 375 nm $SiO_2$ layer and a 675 μm base Si wafer (Figure 2A).

*Preparation of Microplate Platform and Microfluidic Platform*: Microplate platform was based on the conventional transparent 96-wells plate (P96F03N, Sansho, Japan) for static measurement. Microfluidic platform was assembled by a PDMS microfluidic chip and a normal substrate (a $SiO_2$ layer and a base Si wafer without the Si-nanocolumns array) for dynamic detection. Microfluidic configuration remained consistent across microfluidic platform and metasurface platform.

*Microfluidic Flowing Program*: The microfluidic flowing program was divided into the following steps: control of reagent flow time and rate, multiple reagents switching, FL imaging and system cleaning and drying. In order to achieve the multiple immobilizations on Si-nanorods, different sample liquids needed to be injected step by step through stainless-steel pins connected to the external inlet and outlet tubes for passing over six metasurface regions where flowing variation among different channels was ≈5%. First, PBS buffer was prepared for 3 min preflow with the flowing rate of 102.8 μL $min^{-1}$ to fill the microfluidic paths. Second, Cys-SA was flowed at 10.9 μL $min^{-1}$ on metasurface area for 11 min and PBS rinse was performed at the flowing rate of 18 μL $min^{-1}$ for ≈7 min. Afterward, FL background measurements were recorded in PBS environment. Next, Biotin-HSA Ab was also performed to flow at 10.9 μL $min^{-1}$ for 11 min then PBS rinsing at 18 μL $min^{-1}$ for 7 min. The same step was repeated when the prepared mixture solution of FL biosensor TPE-4TA and HSA flowed on the Si-nanocolumn array (using PBS-T buffer for rinsing instead of PBS buffer). Ultimately, actual FL images were captured then analyzed by deducting the preceding background effects. Besides, system cleaning would be carried out with neutral washing solutions and pure water for two sections (rinse cleaning of tubes and ultrasonic cleaning of microfluidic chips & metasurface substrates) after FL measurement. Overall, this microfluidic flowing program required ≈70 min flowing process, 30 min FL measurement, and 50 min cleaning and drying, respectively.

*FL Measurement*: In FL setup, UV LED emitted 360 nm excitation light, which focused on the metasurface through an objective lens of numerical aperture (NA) 0.28. After that, beam splitter filtered out the reflected light with the wavelength less than 409 nm, meanwhile emissive FL was collected by objective lens, and transmitted toward a 529–571 nm bandpass filter, then was detected eventually by an uncooled CCD camera. The exposure time was appropriately adjusted according to different platforms and the gain was fixed at 10 during every experiment. The excitation wavelength was set to 360 nm and the emission wavelength was detected within the range of 529–571 nm.

## Supporting Information

Supporting Information is available from the Wiley Online Library or from the author.

## Acknowledgements

Q.H. gratefully acknowledges the financial support from the Flinders University Research scholarship (FURS), and International Cooperative Graduate Program (ICGP) Fellowship under the Flinders University – NIMS Cooperative Graduate Program. M.I. thanks for financial support from the NIMS Priority Research Project "Biomaterials" and JSPS KAKAENHI Grant Number JP24K01389. This study was supported in part by Advanced Research Infrastructure for Materials and Nanotechnology (ARIM) of the MEXT, Japan (Proposal Number JPMXP1223NM5163) and by the supercomputing resources in Cyberscience Centre, Tohoku University, Japan. The authors thank AIEgen Biotech Co., Ltd (Hong Kong) for supplying TEP-4TA for this study.

Open access publishing facilitated by Flinders University, as part of the Wiley - Flinders University agreement via the Council of Australian University Librarians.

## Conflict of Interest

The authors declare no conflict of interest.

## Data Availability Statement

The data that support the findings of this study are available on request from the corresponding author. The data are not publicly available due to privacy or ethical restrictions.

## Keywords

AIE FL biosensors, HSA detection, metasurface platform, multi-level immobilizations, Si-nanocolumns

Received: March 30, 2024
Revised: May 14, 2024
Published online: June 4, 2024

[1] J. Hu, S. Bandyopadhyay, Y.-H. Liu, L.-Y. Shao, *Front Phys* **2021**, *8*, 586087.
[2] J. Canet-Ferrer, *Metamaterials and metasurfaces*, (Ed: J. Canet-Ferrer), BoD–Books on Demand, Norderstedt, Germany **2019**.
[3] A. Ali, A. Mitra, B. Aïssa, *Nanomaterials* **2022**, *12*, 1027.
[4] H. H. Hsiao, C. H. Chu, D. P. Tsai, *Small Methods* **2017**, *1*, 1600064.
[5] P. Gutruf, C. Zou, W. Withayachumnankul, M. Bhaskaran, S. Sriram, C. Fumeaux, *ACS Nano* **2016**, *10*, 133.
[6] L. Li, T. Jun Cui, W. Ji, S. Liu, J. Ding, X. Wan, Y. Bo Li, M. Jiang, C.-W. Qiu, S. Zhang, *Nat Commun* **2017**, *8*, 197.
[7] H.-S. Ee, R. Agarwal, *Nano Lett.* **2016**, *16*, 2818.
[8] A. V. Kabashin, P. Evans, S. Pastkovsky, W. Hendren, G. A. Wurtz, R. Atkinson, R. Pollard, V. A. Podolskiy, A. V. Zayats, *Nat. Mater.* **2009**, *8*, 867.
[9] M. L. Tseng, Y. Jahani, A. Leitis, H. Altug, *ACS Photonics* **2020**, *8*, 47.
[10] H. Zhu, S. Cheung, K. L. Chung, T. I. Yuk, *IEEE Trans Antennas Propag* **2013**, *61*, 4615.
[11] M. Farmahini-Farahani, H. Mosallaei, *Opt. Lett.* **2013**, *38*, 462.
[12] Y. Bao, X. Ren, S. Liao, Q. Xue, *ACS Appl. Mater. Interfaces* **2023**, *15*, 40022.
[13] S. Zhang, C. L. Wong, S. Zeng, R. Bi, K. Tai, K. Dholakia, M. Olivo, *Nanophotonics* **2020**, *10*, 259.
[14] R. Liu, X. Ye, T. Cui, *Research* **2020**, *2020*, 7949037.
[15] I. O. Oguntoye, B. K. Simone, S. Padmanabha, G. Z. Hartfield, P. Amrollahi, T. Y. Hu, A. J. Ollanik, M. D. Escarra, *ACS Appl. Nano Mater.* **2022**, *5*, 3983.
[16] Y. Wang, M. A. Ali, E. K. Chow, L. Dong, M. Lu, *Biosens. Bioelectron.* **2018**, *107*, 224.
[17] A. Negm, M. M. Howlader, M. Bakr, S. Ali, *Mater. Des.* **2023**, *227*, 111747.
[18] M. Iwanaga, *ACS Nano* **2020**, *14*, 17458.
[19] M. Iwanaga, *Biosensors* **2023**, *13*, 377.
[20] M. Iwanaga, T. Hironaka, N. Ikeda, T. Sugasawa, K. Takekoshi, *Nano Lett.* **2023**, *23*, 5755.
[21] S. Cheung, B. Guan, S. Djordjevic, K. Okamoto, S. Yoo, *2012 Conference on Lasers and Electro-Optics (CLEO)*, IEEE, San Jose, CA, USA **2012**.
[22] F. Van Laere, T. Claes, J. Schrauwen, S. Scheerlinck, W. Bogaerts, D. Taillaert, L. O'Faolain, D. Van Thourhout, R. Baets, *IEEE Photonics Technol. Lett.* **2007**, *19*, 1919.
[23] J. Ferrara, W. Yang, L. Zhu, P. Qiao, C. J. Chang-Hasnain, *Opt. Express* **2015**, *23*, 2512.
[24] Y. Hong, J. W. Lam, B. Z. Tang, *Chem. Soc. Rev.* **2011**, *40*, 5361.
[25] X. Zhang, B. Yao, Q. Hu, Y. Hong, A. Wallace, K. Reynolds, C. Ramsey, A. Maeder, R. Reed, Y. Tang, *Mater. Chem. Front.* **2020**, *4*, 2548.
[26] Q. Hu, B. Yao, T. C. Owyong, S. Prashanth, C. Wang, X. Zhang, W. W. Wong, Y. Tang, Y. Hong, *Chem Asian J* **2021**, *16*, 1245.
[27] A. R. Dyer, P. Greenland, P. Elliott, M. L. Daviglus, G. Claeys, H. Kesteloot, H. Ueshima, J. Stamler, *Am J Epidemiol* **2004**, *160*, 1122.
[28] J. A. Simerville, W. C. Maxted, J. J. Pahira, *Am. Fam. Physician* **2005**, *71*, 1153.
[29] S. Bouatra, F. Aziat, R. Mandal, A. C. Guo, M. R. Wilson, C. Knox, T. C. Bjorndahl, R. Krishnamurthy, F. Saleem, P. Liu, *PLoS One* **2013**, *8*, e73076.
[30] A. Birková, J. Oboril, R. Kréta, B. Čižmárová, B. Hubková, Z. Šteffeková, J. Genči, J. Paralič, M. Mareková, *Biomed Signal Process Control* **2020**, *56*, 101693.
[31] H. P. Patel, *Pediatr Clin North Am* **2006**, *53*, 325.
[32] S. Aitekenov, A. Gaipov, R. Bukasov, *Talanta* **2021**, *223*, 121718.
[33] B. Choi, M. Iwanaga, H. T. Miyazaki, Y. Sugimoto, A. Ohtake, K. Sakoda, *Chem. Commun.* **2015**, *51*, 11470.
[34] M. Iwanaga, B. Choi, H. T. Miyazaki, Y. Sugimoto, *Nanoscale* **2016**, *8*, 11099.
[35] M. Iwanaga, *Appl. Sci.* **2018**, *8*, 1328.
[36] M. Iwanaga, *Plasmonic Resonators: Fundamentals, Advances, and Applications*, Jenny Stanford Publishing, New York **2016**.
[37] A. Irrera, A. A. Leonardi, C. Di Franco, M. J. Lo Faro, G. Palazzo, C. D'Andrea, K. Manoli, G. Franzo, P. Musumeci, B. Fazio, *ACS Photonics* **2018**, *5*, 471.
[38] Y. Tu, Y. Yu, Z. Zhou, S. Xie, B. Yao, S. Guan, B. Situ, Y. Liu, R. T. Kwok, J. W. Lam, *ACS Appl. Mater. Interfaces* **2019**, *11*, 29619.
[39] Z. Luo, B. Liu, K. Zhu, Y. Huang, C. Pan, B. Wang, L. Wang, *Dyes Pigm.* **2018**, *152*, 60.
[40] Y. Huang, T. Lv, T. Qin, Z. Xu, L. Wang, B. Liu, *Chem. Commun.* **2020**, *56*, 11094.
[41] K. Zhu, T. Lv, T. Qin, Y. Huang, L. Wang, B. Liu, *Chem. Commun.* **2019**, *55*, 13983.
[42] A. Zorzi, S. Linciano, A. Angelini, *MedChemComm* **2019**, *10*, 1068.
[43] M. Fasano, S. Curry, E. Terreno, M. Galliano, G. Fanali, P. Narciso, S. Notari, P. Ascenzi, *IUBMB Life* **2005**, *57*, 787.
[44] L. Santucci, G. Candiano, A. Petretto, M. Bruschi, C. Lavarello, E. Inglese, P. G. Righetti, G. M. Ghiggeri, *J. Proteomics* **2015**, *112*, 53.
[45] A. Marimuthu, R. N. O'Meally, R. Chaerkady, Y. Subbannayya, V. Nanjappa, P. Kumar, D. S. Kelkar, S. M. Pinto, R. Sharma, S. Renuse, *J. Proteome Res.* **2011**, *10*, 2734.
[46] M. Iwanaga, W. Tangkawsakul, *Biosensors* **2022**, *12*, 981.
[47] M. Iwanaga, *Biosensors* **2022**, *12*, 987.
[48] M. Iwanaga, *Biosens. Bioelectron.* **2021**, *190*, 113423.